# Checkpoint Nano-PROTACs for Activatable Cancer Photo-immunotherapy

*Chi Zhang, Mengke Xu, Shasha He, Jingsheng Huang, Cheng Xu, and Kanyi Pu**

Dr. C. Zhang, M. Xu, Dr. S. He, J. Huang, C. Xu, Prof. K. Pu
School of Chemistry, Chemical Engineering and Biotechnology, Nanyang Technological University, 70 Nanyang Drive, 637457, Singapore

Prof. K. Pu
Lee Kong Chian School of Medicine, Nanyang Technological University, 59 Nanyang Drive, 636921, Singapore
E-mail: kypu@ntu.edu.sg

**Keywords:** Phototherapy, PROTAC, cancer immunotherapy, checkpoint blockade

## Abstract

Checkpoint immunotherapy holds great potential to treat malignancies via blocking the immunosuppressive signaling pathways, which however suffers from inefficiency and off-target adverse effects. We herein report checkpoint nano-proteolysis targeting chimeras (nano-PROTACs) in combination with photodynamic tumor regression and immunosuppressive protein degradation to block checkpoint signaling pathways for activatable cancer photo-immunotherapy. These nano-PROTACs are composed of a photosensitizer (protoporphyrin IX, PpIX) and an Src homology 2 domain-containing phosphatase 2 (SHP2)-targeting PROTAC peptide (aPRO) via a caspase 3-cleavable segment. aPRO is activated by the increased expression of caspase 3 in tumor cells after phototherapeutic treatment and induces targeted degradation of SHP2 via the ubiquitin-proteasome system. The persistent depletion of SHP2 blocks the immunosuppressive checkpoint signaling pathways (CD47/SIRPα and PD-1/PD-L1), thus reinvigorating antitumor macrophages and T cells. Such a checkpoint PROTAC strategy synergizes immunogenic phototherapy to boost antitumor immune response. Thus, this study represents a generalized PROTAC platform to modulate immune-related signaling pathways for improved anticancer therapy.

## 1. Introduction

Cancer immunotherapy is an emerging strategy to treat malignancies by reinvigorating the intrinsic immune system, especially cytotoxic T lymphocytes and phagocytes.[1] Among these immunotherapeutic strategies, immune checkpoint blockade has achieved impressive success owing to the significantly increased clinical benefit in patients with melanoma.[2] Despite these advances, the current checkpoint blockade immunotherapies still suffer from limited response rates in specific malignancies and immune-related adverse events (irAEs) in the clinic.[3] Cancer nanomedicines in combination with checkpoint blockade immunotherapy have shown great potential to improve antitumor immune response in a safe and effective manner owing to their good biocompatibility and tumor-targeted accumulation capability.[4] Activatable cancer nanomedicines afford further opportunities to specifically modulate antitumor immune response with decreased irAEs in the presence of external stimuli (e.g., light, heat, ultrasound, or magnetic field) or cancer biomarkers.[5] Moreover, many conventional cancer treatment modalities, such as chemotherapy, radiotherapy, sonodynamic, photodynamic, and photothermal therapy, can trigger immunogenic cell death, which have been reported to sensitize tumors to checkpoint blockade immunotherapy with improved antitumor efficacy.[6] For example, a nano-liposome encapsulating the sonosensitizer (hematoporphyrin monomethyl ether) and a toll-like receptor-7 agonist (imiquimod) with the combination of anti-programmed death ligand 1 (anti-PD-L1) checkpoint blockade has been utilized to inhibit tumor growth with high efficacy,[7] and a nanocomplex loaded with paclitaxel, CXCR4 antagonism, and anti-PD-L1 small interfering RNA is developed to treat lung tumors for effective immunotherapy.[8] These studies validated the great potential of activatable nanomedicine-based combinational cancer immunotherapy in the treatment of malignancies.

PROTAC (proteolysis targeting chimera), a promising protein degradation technology, has been exploited to knock out the targeted protein for disease treatment.[9] The heterobifunctional structure of PROTAC offers the binding specificity to both targeted proteins and intracellular E3 ligases, thus leading to targeted protein degradation via the ubiquitin-proteasome system (UPS).[10] Compared with small molecule inhibitors or genetic tools, PROTAC exhibits a higher protein degradation efficiency with persistent and recyclable action.[11] Thus, PROTAC has been utilized to degrade many undruggable oncoproteins (e.g., signal transducer and activator of transcription 3, K-Ras, protein tyrosine phosphatase, etc.) for enhanced cancer therapy.[12] However, PROTAC-based specific degradation of immune checkpoint ligands and receptors has been rarely reported owing to the limited accessibility of membrane-bound proteins by the cytosolic UPS.[13] Therefore, developing an immune checkpoint PROTAC to promote the antitumor immune response is urgently needed.

Herein, we develop a checkpoint nano-PROTAC (NPRO) targeting the Src homology 2 domain-containing phosphatase 2 (SHP2) for activatable cancer photo-immunotherapy (**Figure 1**). NPRO is synthesized via the self-assembly of the blocked PROTAC (bPRO) peptide, which comprises the photosensitizer (protoporphyrin IX, PpIX), the caspase 3-cleavable peptide substrate (DEVD),[14] the UBR E3 ligase targeting segment (RLAA),[15] and the SHP2-targeting peptide (SP, SLNpYIDLDLVK).[16] After systemic administration, NPRO accumulates at tumor sites via the enhanced penetration and retention effect. Under 660 nm photoirradiation, NPRO generates $^1O_2$ to eliminate tumor cells, which induces immunogenic cell death (ICD) via tumor-associated antigens (TAAs) release and the enhanced expression of caspase 3 in tumor cells. The overexpressed caspase 3 further facilitates the cleavage of DEVD and leads to the release of activated PROTAC (aPRO). aPRO specifically binds to SHP2 and the UBR proteins (an E3 ubiquitin ligase) via the SP segment and the UBR E3 ligase targeting segment, respectively, leading to persistent degradation of SHP2 via the ubiquitin-proteasome system. The depletion of SHP2 blocks the immunosuppressive signals including CD47/SIRPα ("Don't eat me") and PD-1/PD-L1 signals,[17] resulting in the activation of M1-type macrophages (M1

Macs)-mediated phagocytosis effect and effector T cells (Teffs)-mediated antitumor immunity. Moreover, the combinational cancer photo-immunotherapy with immunosuppressive SHP2 degradation induces the repolarization of M2-type macrophages (M2 Macs) to M1 Macs and promotes the infiltration of activated Teffs into tumor microenvironment. As a result, the checkpoint NPRO exerts synergistic antitumor effects via activatable cancer photo-immunotherapy.

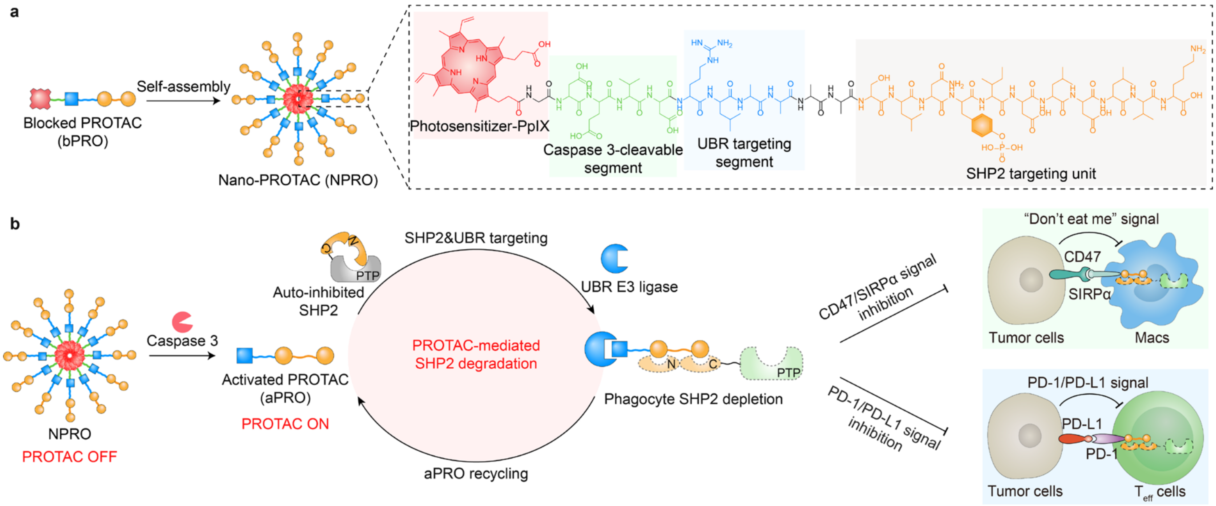

**Figure 1.** Schematic illustration of checkpoint nano-PROTACs for activatable cancer photo-immunotherapy. (a) Synthesis and chemical structure of nano-PROTACs (NPRO). (b) Mechanistic illustration of NPRO-mediated activatable cancer photo-immunotherapy: i) Caspase 3-specific activation of NPRO for persistent Src homology-2 domain-containing protein tyrosine phosphatase-2 (SHP2) degradation via specifically binding SHP2 and UBR E3 ligase; ii) SHP2 degradation-mediated inhibition of CD47/SIRPα ("Don't eat me") signals in macrophages (Macs) leading to enhanced phagocytosis effects; iii) SHP2 degradation-mediated inhibition of PD-1/PD-L1 signals in T cells leading to enhanced antitumor T-cell immunity.

## 2. Results and Discussion

NPRO was obtained via the self-assembly of the amphiphilic bPRO peptide in PBS solution. And bPRO was synthesized using the solid-phase peptide synthesis (SPPS) method (Figure S1, Supporting Information).[18] After repeated peptide coupling steps, the photosensitizer PpIX was finally conjugated to the peptide via the SPPS method. In contrast, SP, aPRO, and caspase 3-cleavable segment-containing aPRO (cPRO) were prepared via a similar method and characterized by electrospray ionization-mass spectrometry (ESI-MS, Figures S2-S6, Supporting Information).

The physical and optical properties of SP, aPRO, cPRO, and NPRO were further investigated. NPRO exhibited a small particle size (~40 nm) and a uniform size distribution according to transmission electron microscopy (TEM) images (**Figure 2**a). The hydrodynamic particle size of NPRO is ~80 nm via the dynamic light scattering (DLS) analysis, which is slightly larger than the TEM results (Figure 2b). In comparison, SP, aPRO, and cPRO exhibited much larger hydrodynamic particle sizes (~400 nm) than NPRO owing to the lack of a hydrophobic PpIX unit for effective self-assembly. The zeta potential analysis further demonstrated the negatively charged particle surface of NPRO (~-10 mV) and other contrast groups (Figure 2c). NPRO exhibited similar UV-vis absorption spectra (characteristic absorption peaks at about 505 nm, 540 nm, 575 nm, and 625 nm) compared with PpIX due to the existence of the photosensitizer unit (PpIX) (Figure 2d). The fluorescence spectra of PpIX and NPRO further exhibited similar characteristic emission peaks at 625 nm and 680 nm (Figure 2e).

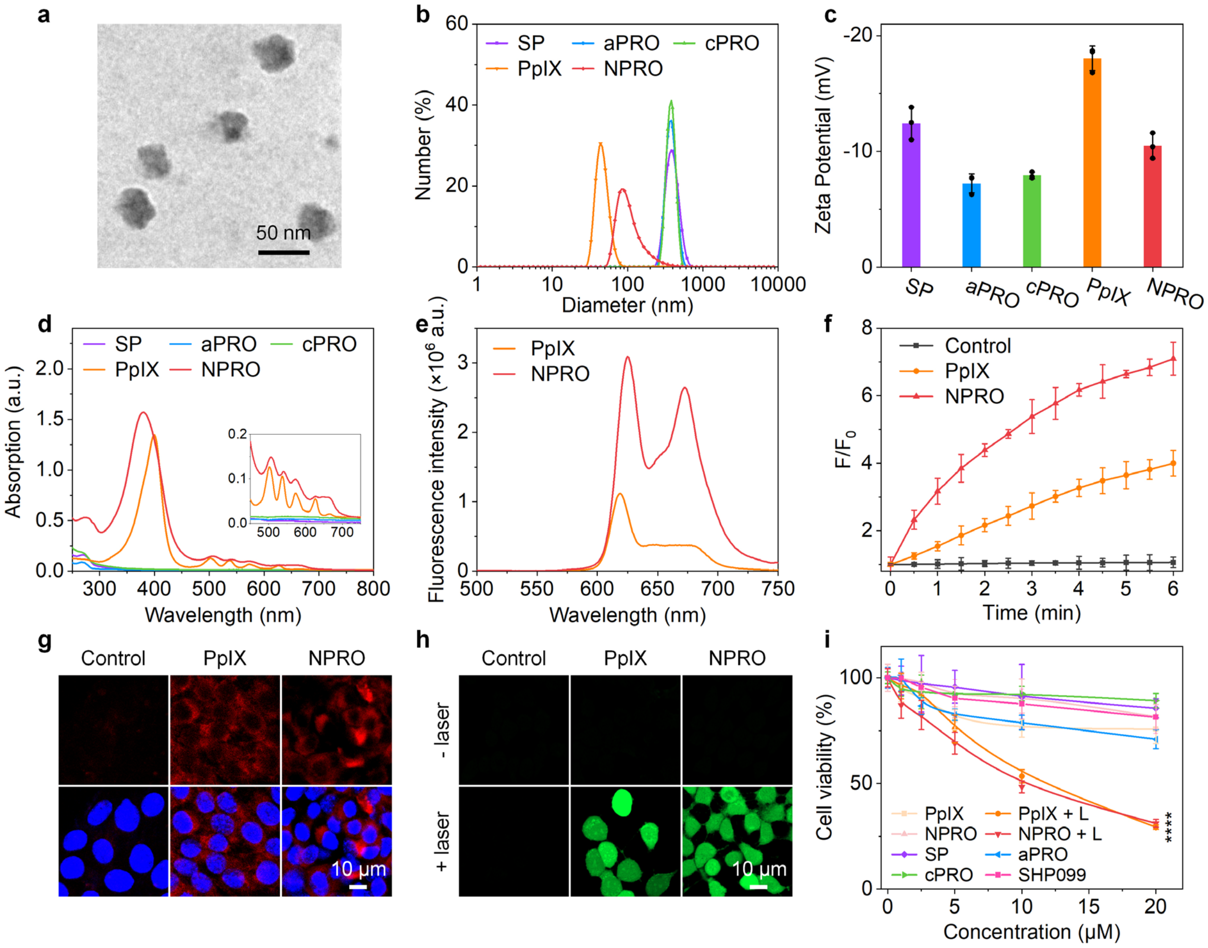

**Figure 2.** Synthesis and characterization of NPRO for activatable cancer photo-immunotherapy. (a) TEM images of NPRO. (b) DLS profiles, (c) Zeta potential, and (d) UV/Vis absorption spectra of SP, aPRO, cPRO, PpIX, and NPRO in PBS solutions. (e) Fluorescence spectra of PpIX and NPRO in PBS solutions. (f) The $^1O_2$ generation profiles of PpIX and NPRO (10 μM) in PBS solution under 660 nm photoirradiation (30 mW/cm$^2$). (g) Confocal fluorescence images of 4T1 cells after 12 h incubation with PpIX and NPRO (10 μM). Blue fluorescence indicated Hoechst 33342 and red fluorescence indicated PpIX. (h) Confocal fluorescence images of 4T1 cells after 12 h incubation with PpIX and NPRO (10 μM) and staining with $H_2$DCFDA with or without 660 nm photoirradiation (30 mW/cm$^2$) for 6 min. Green fluorescence indicated DCF. (i) Cell viabilities of 4T1 cells after 24 h incubation with SHP099, SP, aPRO, cPRO, PpIX, or NPRO at different concentrations with or without 660 nm photoirradiation (30 mW/cm$^2$) for 6

min. PpIX or NPRO with photoirradiation versus without photoirradiation: $p<0.0001$. Statistical significance in (i) was calculated via two-tailed Student's t-test.

The photodynamic activities of NPRO were further investigated. The $^1O_2$ generation was detected using a $^1O_2$ fluorescent probe, singlet oxygen sensor green (SOSG). The fluorescence intensity of SOSG at 525 nm showed a gradual increase under 660 nm photoirradiation with a power intensity of 30 mW/cm$^2$ in a time-dependent manner (Figure 2f). The SOSG fluorescence intensity of NPRO increased by 1.8-fold compared with PpIX after 6 min 660 nm photoirradiation, resulting from the amphiphilic structure and stable self-assembly ability of NPRO in aqueous solutions.

The NPRO-mediated activatable cancer photo-immunotherapy was further investigated in 4T1 murine breast cancer cells. After incubation with PpIX and NPRO for 12 h, 4T1 cells were stained with Hoechst 33342 to study the cellular internalization via confocal fluorescence imaging. Both PpIX- and NPRO-incubated cells exhibited the red fluorescence signals from PpIX (Figure 2g). And the mean fluorescence intensities (MFIs) for PpIX and NPRO were 38.9 and 47.7, respectively (Figure S7, Supporting Information). These results demonstrated the effective cellular uptake abilities of PpIX and NPRO.

The photodynamic activity and cytotoxicity of PpIX and NPRO in 4T1 cells were further studied. The intracellular reactive oxygen species (ROS) generation was detected by using the ROS fluorescent turn-on probe 2',7'-dichlorodihydrofluorescein diacetate ($H_2$DCFDA). After cellular uptake, $H_2$DCFDA can be hydrolyzed by the intracellular esterase in 4T1 cells and oxidized into the fluorescent 2',7'-dichlorofluorescein (DCF) by ROS.[19] Obvious green fluorescence signals from DCF were detected in both PpIX- and NPRO-incubated 4T1 cells after 660 nm photoirradiation for 6 min according to the confocal fluorescence images (Figure 2h). The DCF MFIs of PpIX- and NPRO-incubated cells increased by 105.2- and 90.9-fold compared with the unirradiated cells, respectively, indicating their effective ROS generation abilities under 660 nm photoirradiation. The cytotoxicity of SHP099 (an SHP2 inhibitor),[20] SP, aPRO, cPRO, PpIX, and NPRO was then evaluated using the MTS (3-(4,5-dimethylthiazol-2-yl)-5-(3-carboxymethoxyphenyl)-2-(4-sulfophenyl)-2H-tetrazolium) cell viability assay. The cell viabilities were above 80% in SHP099-, SP-, aPRO-, cPRO-, PpIX-, and NPRO-incubated 4T1 cells without 660 nm photoirradiation, demonstrating their negligible cytotoxicity (Figure 2i). The cytotoxicity of PpIX- and NPRO-incubated cells increased in a concentration-dependent manner under 660 nm photoirradiation. The cell viabilities of PpIX- and NPRO-incubated and photoirradiated cells similarly decreased to ~30% at the concentration of 20 μM. These results indicated that PpIX and NPRO had remarkable phototherapeutic abilities under 660 nm photoirradiation.

The intracellular SHP2 expression was further studied via immunofluorescence imaging. M2 Macs and CD8$^+$ T cells were incubated with SHP099, SP, aPRO, cPRO, PpIX, or NPRO for 12 h, followed by staining with anti-SHP2 antibodies for immunofluorescence imaging. The green fluorescence signals from the anti-SHP2 antibodies in aPRO-incubated M2 Macs or CD8$^+$ T cells were weaker than the other groups (**Figure 3**a). Compared with the control cells, the MFIs of the anti-SHP2 antibodies in aPRO-treated M2 Macs or CD8$^+$ T cells greatly decreased by 72.8% and 95.3% (Figure 3b). In contrast, the incubation of M2 Macs or CD8$^+$ T cells with SHP099, SP, cPRO, PpIX, or NPRO did not decrease the MFIs of anti-SHP2 antibodies. These results indicated that only aPRO treatment could induce the degradation of SHP2 due to the PROTAC-mediated repeated protein degradation ability.

To further investigate the mechanism of caspase 3-mediated NPRO activation, we incubated M2 Macs or CD8$^+$ T cells with 4T1 cell supernatants after various treatments to evaluate SHP2 expression via immunofluorescence imaging. We first treated 4T1 cells with or without caspase 3 inhibitor (Cas3i, Ac-DEVD-CHO) and incubated them with SHP099, SP, aPRO, cPRO, PpIX, or NPRO for 12 h. The cells were then treated with 660 nm photoirradiation for 6 min and incubated for another 12 h to collect the cell supernatants. M2 Macs or CD8$^+$ T cells were further incubated with these cell supernatants for 12 h, followed by staining with anti-SHP2 antibodies for immunofluorescence imaging. The green fluorescence signals from the anti-SHP2 antibodies in M2 Macs or CD8$^+$ T cells incubated with aPRO- or NPRO + L-treated 4T1 cell supernatants were obviously weaker than the other groups. These data verified that NPRO could convert into active aPRO and further transfer to macrophages or T cells in the presence of caspase 3 during photodynamic therapy-induced apoptosis of 4T1 cells (Figure S8, Supporting Information). In contrast, the SHP2 immunofluorescence signals in M2 Macs or CD8$^+$ T cells with NPRO + L + Cas3i treatment did not exhibit obvious changes compared with NPRO group. These results confirmed that NPRO could be activated by the apoptosis-associated caspase 3 to induce SHP2 degradation and Cas3i treatment could disable the SHP2 degradation ability of NPRO.

Afterward, SHP099-, SP-, cPRO-, aPRO-, PpIX-, and NPRO-treated M2 Macs or CD8$^+$ T cells were incubated with 4T1 cells to verify the activation and phagocytosis efficiency of these immune cells. We first investigated the repolarization ability of immunosuppressive M2 Macs into inflammatory M1 Macs via flow cytometry analysis. The populations of M1 Macs were 28.7% and 32.7% after the incubation with SHP099 and aPRO owing to the inhibition and degradation of SHP2, respectively (Figure S9, Supporting Information). In contrast, the other groups exhibited much lower populations (~20%) of M1 Macs. Then, the phagocytosis efficiency was studied by the coincubation of carboxyfluorescein succinimidyl ester (CFSE)-labeled 4T1 cells with M2 Macs of different treatments (Figure 3c). The SHP099 and aPRO groups exhibited 49.7% and 46.8% phagocytosis efficiencies respectively, which are much higher than the other groups (less than 20%). The activation of cytotoxic T cells (granzyme B$^+$ (GranB$^+$) or IFN-$\gamma^+$) was further studied by the coincubation of 4T1 cells with CD8$^+$ T cells of different treatments. The populations of GranB$^+$CD8$^+$ T cells were 18.9% and 45.2% in SHP099 and aPRO groups, respectively (Figure 3d), which are higher than the other groups (~10%). Similarly, IFN-γ$^+$CD8$^+$ T cells exhibited higher populations in SHP099 (20.1%) and aPRO (35.1%) groups compared with the other groups (Figure S10, Supporting Information). Moreover, the extracellular concentrations of TNF-α and IFN-γ in aPRO-treated T cells were also increased by 1.5 and 2.2 folds compared with the control groups, respectively (Figure 3e and 3f). Importantly, the aPRO group exhibited higher T cell activation efficiencies (GranB$^+$CD8$^+$ and IFN-γ$^+$CD8$^+$) and cytokine levels (TNF-α and IFN-γ) than the SHP099 group, which demonstrated the robust activation of T cells via the PROTAC-mediated degradation of SHP2.

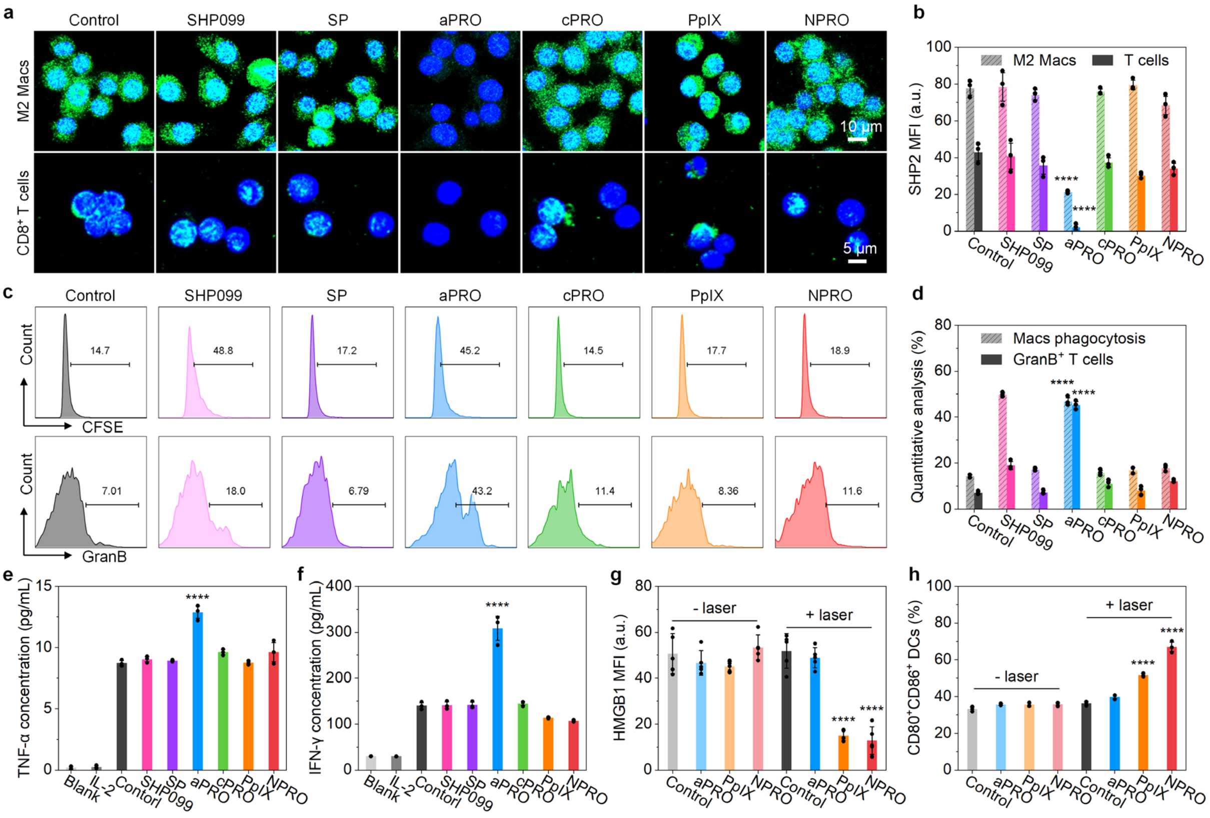

**Figure 3.** In vitro NPRO-mediated activatable cancer photo-immunotherapy. (a) Confocal fluorescence images and (b) MFIs of M2 Macs and CD8$^+$ T cells after incubation with SHP099, SP, aPRO, cPRO, PpIX, and NPRO for 12 h (*n*=3). Blue fluorescence indicated Hoechst 33342, and green fluorescence showed the anti-SHP2 antibodies. aPRO versus control for M2 Macs or

T cells: $p<0.0001$. (c) Flow cytometry and (d) quantitative analysis of Macs phagocytosis and GranB$^+$CD8$^+$ T cell activation after coincubation of SHP099-, SP-, aPRO-, cPRO-, PpIX-, and NPRO-treated M2 Macs or CD8$^+$ T cells with 4T1 cells for 24 h ($n$=3). aPRO versus control for Macs phagocytosis or GranB$^+$ T cells: $p<0.0001$. (e) TNF-α and (f) IFN-γ assay after coincubation of SHP099-, SP-, aPRO-, cPRO-, PpIX-, and NPRO-treated CD8$^+$ T cells with 4T1 cells for 24 h ($n$=3). aPRO versus control for TNF-α or IFN-γ: $p<0.0001$. (g) MFIs of aPRO-, PpIX-, and NPRO-incubated 4T1 cells with or without 660 nm photoirradiation (30 mW/cm$^2$) for 6 min ($n$=5). PpIX or NPRO versus control: $p<0.0001$. (h) Quantification of the matured DCs (CD80$^+$CD86$^+$) after the incubation of BMDCs with the 4T1 cell supernatants after different treatments for 12 h ($n$=3). 4T1 cells were incubated with aPRO, PpIX, and NPRO with or without 660 nm photoirradiation (30 mW/cm$^2$) for 6 min. PpIX or NPRO versus control: $p<0.0001$. Statistical significance in (b,d), and (e-h) was calculated via one-way ANOVA with a Tukey post-hoc test.

The ability to induce ICD and dendritic cell (DC) maturation was further investigated in 4T1 cells. High-mobility group protein B1 (HMGB1), one of the important biomarkers to evaluate ICD, was detected via immunofluorescence imaging.[21] The HMGB1 expression in 4T1 cell nuclei was detected via immunofluorescence imaging. In NPRO-incubated 4T1 cells without photoirradiation, there was an obvious overlap of the green fluorescence signals from anti-HMGB1 antibodies with the blue fluorescence signals from the cell nuclear dye (Hoechst 33342) (Figure S11, Supporting Information). The MFIs of anti-HMGB1 antibodies in PpIX- and NPRO-incubated and photoirradiated cells greatly decreased by 66.7% and 76.0% relative to the unirradiated cells, indicating the effective release of HMGB1 from cell nuclei to the cell supernatants (Figure 3g). These data demonstrated that PpIX- and NPRO-mediated phototherapy similarly induced ICD. Afterward, DC maturation was evaluated via flow cytometry analysis. Bone marrow-derived dendritic cells (BMDCs) were incubated with the supernatants of 4T1 cells after different treatments. After 12 h incubation, the proportions of matured DCs ($CD80^+CD86^+$) were 51.7% and 67.0% after incubation with PpIX- and NPRO-treated and photoirradiated 4T1 cell supernatants, which were much higher than the other groups (Figure 3h and Figure S12, Supporting Information). Thus, these results demonstrated that NPRO-mediated therapy could induce ICD of tumors and DC maturation to improve tumor immunogenicity and enhance antitumor immune response.

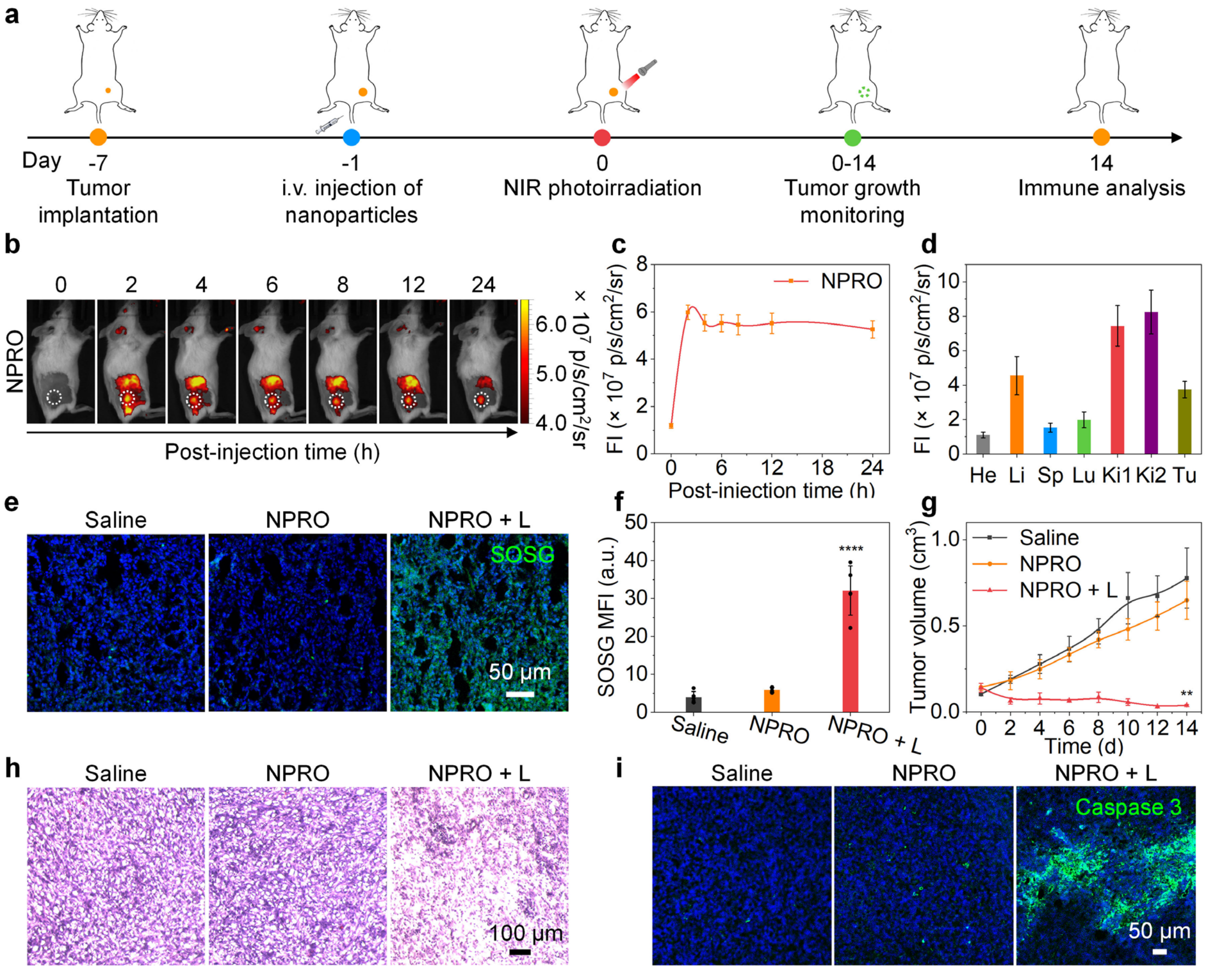

**Figure 4.** In vivo NPRO-mediated activatable cancer photo-immunotherapy. (a) Timeline of 4T1 tumor model establishment and NPRO-mediated activatable cancer photo-immunotherapy. (b) In vivo NIR fluorescence images and (c) quantitative NIR FI of the tumors from 4T1 tumor-bearing mice at the different time points after the intravenous injection of NPRO (200 μL, 1 mM, *n*=3). (d) Quantitative NIR FI of the tumors and major organs from 4T1 tumor-bearing

mice at 24 h post-injection of NPRO (*n*=3). (e) Confocal fluorescence images and (f) SOSG MFIs of the tumor tissues from 4T1 tumor-bearing with or without 660 nm photoirradiation (30 mW/cm$^2$) for 6 min (*n*=3). Blue fluorescence indicated DAPI, and green fluorescence indicated SOSG. NPRO + L versus saline: $p$<0.0001. (g) Tumor growth curves during 14-day monitoring (*n*=5). NPRO + L versus NPRO or saline: $p$<0.01. (h) Histological H&E staining of tumor tissues. (i) Caspase 3 immunofluorescence images of the tumor tissues. Blue fluorescence indicated DAPI, and green fluorescence indicated anti-caspase 3 antibodies. Statistical significance in (g) was calculated via two-tailed Student's t-test. Statistical significance in (f) was calculated via one-way ANOVA with a Tukey post-hoc test.

NPRO-mediated activatable cancer photo-immunotherapy was further studied in the immunocompetent 4T1 tumor-bearing mice. After different treatments of the 4T1 tumor-bearing mice, the tumor growth was monitored, and the immunotherapeutic efficiency was investigated (**Figure 4**a). First, the tumor-targeted accumulation of NPRO was studied using an IVIS imaging system to verify the optimal timepoints for photoirradiation. The fluorescence signals from the PpIX unit gradually increased at tumor sites in NPRO-injected mice (Figure 4b). The fluorescence intensity (FI) reached a maximum value at 6 h post-injection time (Figure 4c). The ex vivo NIR fluorescence images further indicated that NPRO could efficiently accumulate at tumor sites (Figure 4d and Figure S13, Supporting Information). These data indicated that NPRO had a good tumor-targeted accumulation ability due to the small particle size.

The NPRO-mediated cancer photo-immunotherapy was investigated with localized 660 nm photoirradiation after 6 h post-injection of NPRO (the maximum tumor accumulation timepoint). To minimize the photothermal heating effect on mice, the 660 nm photoirradiation was controlled at the safe range with a power intensity of 30 mW/cm$^2$ for 6 min to ensure that the temperature of tumors was below the threshold temperature (43 °C). Then the $^1O_2$ generation was studied by intratumoral injection of SOSG and detection of the fluorescence signals from the oxidized SOSG. In the tumor tissues of NPRO-injected and photoirradiated mice, obvious green fluorescence signals from SOSG were detected (Figure 4e). The MFIs in the tumor tissues of NPRO-injected and photoirradiated mice increased by 8.0- and 5.5-fold compared with the saline- and NPRO-injected mice without photoirradiation, respectively (Figure 4f). These data indicated that NPRO-mediated therapy could induce effective $^1O_2$ generation in tumor tissues after 660 nm photoirradiation.

Afterward, the tumor growths in 4T1 tumor-bearing mice with different treatments were monitored every 2 days to study the in vivo antitumor effects. The most effective inhibition of tumor growth was observed in NPRO-injected and photoirradiated mice relative to the other groups (Figure 4g). H&E staining images of tumor tissues further indicated the obvious dead tumor cells in NPRO-injected and photoirradiated mice compared with the other groups (Figure 4h). Moreover, the caspase 3 immunofluorescence images of tumor tissues in NPRO-injected and photoirradiated mice exhibited obvious green fluorescence signals with the highest MFIs of anti-caspase-3 antibodies compared with the other groups (Figure 4i and Figure S14, Supporting Information). These data verified that NPRO-mediated photo-immunotherapy exhibited the most effective tumor therapeutic efficacy among all the groups.

The biosafety of NPRO was further evaluated via body weight monitoring and histological detection of the major organs. No obvious changes of the mice body weight in different groups were observed during 14-day monitoring during 14-day monitoring (Figure S15, Supporting Information). And the physiological morphologies of H&E staining images of the major organs (including heart, liver, spleen, lung, and kidney) from the mice with different groups remained similar (Figure S16, Supporting Information). These data further verified the high biosafety and biocompatibility of NPRO.

To investigate the mechanism of NPRO-mediated cancer photo-immunotherapy, CD3$^+$CD8$^+$ T cells and CD3$^+$CD8$^+$GranB$^+$ cytotoxic T cells in tumor tissues of the tumor-bearing mice with different treatments were detected via flow cytometry analysis (**Figures 5**a and 5b). The populations of CD3$^+$CD8$^+$ T cells and CD3$^+$CD8$^+$GranB$^+$ cytotoxic T cells in tumors of NPRO-injected and photoirradiated mice were 33.0% and 43.7%, respectively, which were much higher than that of the other groups. The blood of NPRO-injected and photoirradiated mice also exhibited higher populations of CD3$^+$CD8$^+$ T cells (43.1%) and CD3$^+$CD8$^+$GranB$^+$ cytotoxic T cells (24.6%) than the other groups (Figure 5c, Figures S17-20, Supporting Information). Moreover, the population of CD44$^+$CD62L$^-$ effector memory T cells (Tems) in tumors from NPRO-injected and photoirradiated mice was higher than the other groups, indicating the enhanced immune memory effects by NPRO-mediated therapy (Figure S21, Supporting Information). These data demonstrated that NPRO-mediated activatable cancer photo-immunotherapy greatly improved the T cell-mediated antitumor immune response.

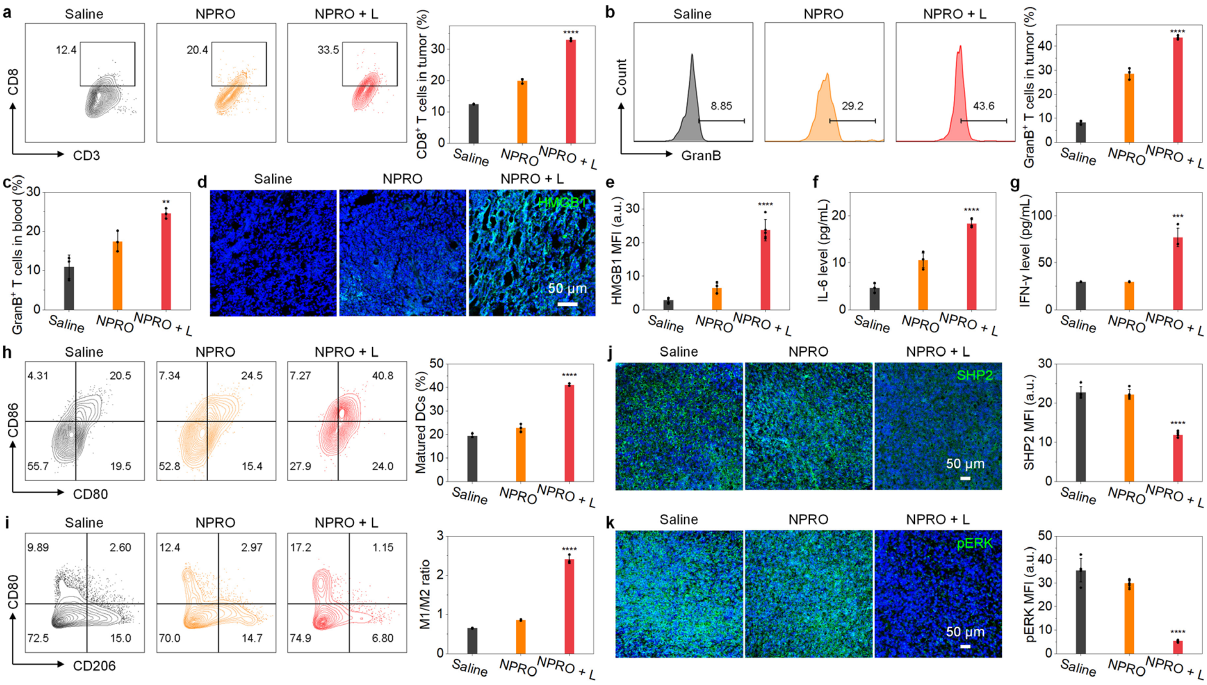

**Figure 5.** In vivo mechanistic study of NPRO-mediated activatable cancer photo-immunotherapy. Flow cytometry and quantitative assay of (a) CD3$^+$CD8$^+$ T cells and (b)

$GranB^+CD8^+$ T cells in the tumors from 4T1 tumor-bearing mice ($n$=3). NPRO + L versus saline: $p$<0.0001. (c) Quantification of $GranB^+CD8^+$ T cells in blood from 4T1 tumor-bearing mice ($n$=3). NPRO + L versus saline: $p$<0.01. (d) HMGB1 immunofluorescence staining images and (e) MFIs of the tumor tissues from 4T1 tumor-bearing mice ($n$=3). Blue fluorescence indicated DAPI, and green fluorescence indicated anti-HMGB1 antibodies. NPRO + L versus saline: $p$<0.0001. In vivo cytokine detection of (f) IL-6 and (g) IFN-γ in sera from 4T1 tumor-bearing mice after different treatments ($n$=3). NPRO + L versus saline in (f): $p$<0.0001; NPRO + L versus saline in (g): $p$<0.001. (h) Flow cytometry assay and quantitative assay of matured DCs ($CD80^+CD86^+$) in TDLNs from 4T1 tumor-bearing mice after different treatments ($n$=3). NPRO + L versus saline: $p$<0.0001. (i) Flow cytometry assay of M1/M2 Macs and quantification of the ratio of M1/M2 Macs in the tumors from 4T1 tumor-bearing mice ($n$=3). NPRO + L versus saline: $p$<0.0001. (j) SHP2 and (k) pERK immunofluorescence staining images and MFIs of the tumor tissues from 4T1 tumor-bearing mice ($n$=3). Blue fluorescence indicated DAPI, and green fluorescence indicated anti-SHP2 or anti-pERK antibodies. NPRO + L versus saline: $p$<0.0001. Statistical significance in (a-c) and (e-k) was calculated via one-way ANOVA with a Tukey post-hoc test.

To further evaluate the antitumor immunity of NPRO-mediated photo-immunotherapy, several immune processes including ICD, cytokine release, and DC maturation of the mice in different groups were studied and compared. The tumoral HMGB1 expression was first detected to evaluate ICD (Figure 5d). The HMGB1 expression in tumor tissues of NPRO-injected and photoirradiated mice exhibited an 8.5-fold increase compared with the saline-injected mice (Figure 5e). The cytokines including interleukine-6 (IL-6) and interferon-γ (IFN-γ) in the serum of the mice in different groups were then detected. The IL-6 and IFN-γ levels in NPRO-injected and photoirradiated mice were 4.0- and 2.6-fold higher than the saline-injected mice, respectively (Figure 5f and 5g). The population of matured DCs in tumor-draining lymph nodes (TDLNs) was detected via flow cytometry analysis to evaluate DC maturation (Figure 5h). The proportion of matured DCs ($CD80^+$ and $CD86^+$) to $CD11c^+$ cells in TDLNs of NPRO-injected and photoirradiated mice increased by 2.1-fold relative to the saline-injected mice. Thus, these results confirmed that NPRO-mediated therapy enhanced tumor immunogenicity owing to the phototherapeutic ability.

To further investigate the antitumor immune response, the tumor-infiltrating macrophages were detected via flow cytometry analysis. The populations of M1 and M2 Macs in the tumor microenvironment from NPRO-injected and photoirradiated mice were 16.7% and 6.9% via flow cytometry assay, respectively (Figure 5i and Figure S22, Supporting Information). The ratios of M1 to M2 Macs in tumors of NPRO-injected and photoirradiated mice were 3.7-fold higher than the saline group (Figure 5i). These data confirmed that NPRO-mediated cancer photo-immunotherapy greatly decreased the immunosuppressive M2 Macs and increased inflammatory M1 Macs.

To further confirm the immunosuppressive signal modulation by NPRO, the SHP2 and phosphorylated ERK1/2 (pERK) expression in tumor tissues were investigated.[22] The SHP2 expression in tumors of NPRO-injected and photoirradiated mice greatly decreased by 47.6% and 46.4% compared with the saline-injected and NPRO-injected mice without photoirradiation, respectively (Figure 5j). Moreover, we detected the expression of SHP2 in M1 Macs and $CD8^+$ T cells of 4T1 tumors via flow cytometry. The population of $SHP2^+$ M1 Macs or $SHP2^+CD8^+$ T cells in 4T1 tumors from NPRO-injected and photoirradiated mice exhibited obvious decreases compared with the saline group (Figure S23, Supporting Information). Meanwhile, the pERK expression in tumors of NPRO-injected and photoirradiated mice decreased by 84.7% and 81.9% relative to the saline-injected and NPRO-injected mice without photoirradiation, respectively (Figure 5k). These data further verified that NPRO-mediated cancer photo-immunotherapy greatly decreased SHP2 and pERK expression in tumors. This should be attributed to the PROTAC-mediated persistent degradation of SHP2 and subsequent inhibition of the immunosuppressive checkpoint signaling pathways (CD47/SIRPα and PD-1/PD-L1). Thus, NPRO-mediated therapy could effectively reprogram the immunosuppressive checkpoint signals and boost the antitumor immune response.

## 3. Conclusion

In summary, we report a checkpoint nano-PROTAC (NPRO) to induce targeted protein (SHP2) degradation in a persistent and controlled manner for modulating the immunosuppressive checkpoint signaling pathways (CD47/SIRPα and PD-1/PD-L1). NPRO represents a unique type of PROTACs that is specifically activated by the overexpressed caspase 3 in apoptotic tumor cells after photodynamic therapy. The activated PROTAC (aPRO) is able to specifically bind to the targeted protein (SHP2) and the UBR E3 ligase in both tumor-infiltrating macrophages and T cells, leading to the degradation of SHP2 via the ubiquitin-proteasome system. The high SHP2-degradation efficiency in both M2 Macs (72.8%) and T cells (95.3%) exhibits great potential to reprogram the immunosuppressive tumor microenvironment owing to the recycled activity of aPRO (Figure 3a-3b). In vitro results confirmed higher populations of M1 Macs (32.7%) and cytotoxic GranB$^{+}$CD8$^{+}$ T cells (45.2%) after the aPRO treatment than that of the SHP099 treatment (28.7% for M1 Macs; 18.9% for T cells) at the same concentration (Figure 3c-3d). The phagocytosis efficiency of aPRO-treated macrophages and the secreted cytokines of aPRO-treated T cells also exhibited high levels compared with the SHP099 treatment (Figure 3c-3f). In vivo results further verified that NPRO-mediated photo-immunotherapy effectively boosted antitumor immune responses by inducing ICD of tumor cells and reprogramming the immunosuppressive checkpoint signaling pathways (CD47/SIRPα and PD-1/PD-L1) via the degradation of SHP2 (Figure 5). To the best of our knowledge, this work represents the first checkpoint PROTACs that can specifically modulate the immunosuppressive checkpoint CD47/SIRPα and PD-1/PD-L1 signaling pathways. Thus, this activatable and checkpoint PROTAC design can be generalized for the modulation of several other checkpoint signaling pathways via the degradation of corresponding enzymes and hold great potential to synergize with other cancer treatment modalities.

## Supporting Information

Supporting Information is available from the Wiley Online Library or from the author.

## Acknowledgments

K.P. thanks Singapore Ministry of Education, Academic Research Fund Tier 1 (2019-T1-002-045, RG125/19), Academic Research Fund Tier 2 (MOE2018-T2-2-042), and A*STAR SERC AME Programmatic Fund (SERC A18A8b0059) for the financial support.

Received: ((will be filled in by the editorial staff))
Revised: ((will be filled in by the editorial staff))
Published online: ((will be filled in by the editorial staff))

## References

[1] a) P. S. Hegde, D. S. Chen, *Immunity* **2020**, *52*, 17; b) M. M. T. van Leent, B. Priem, D. P. Schrijver, A. de Dreu, S. R. J. Hofstraat, R. Zwolsman, T. J. Beldman, M. G. Netea, W. J. M. Mulder, *Nat. Rev. Mater.* **2022**, *7*, 465; c) Q. Chen, M. Chen, Z. Liu, *Chem. Soc. Rev.* **2019**, *48*, 5506.

[2] a) D. A. Braun, Z. Bakouny, L. Hirsch, R. Flippot, E. M. Van Allen, C. J. Wu, T. K. Choueiri, *Nat. Rev. Clin. Oncol.* **2021**, *18*, 199; b) A. Kalbasi, A. Ribas, *Nat. Rev. Immunol.* **2020**, *20*, 25; c) Y. Yang, J. Xu, Y. Sun, L. Mo, B. Liu, X. Pan, Z. Liu, W. Tan, *J. Am. Chem. Soc.* **2021**, *143*, 8391.

[3] a) G. Morad, B. A. Helmink, P. Sharma, J. A. Wargo, *Cell* **2021**, *184*, 5309; b) L. Galluzzi, J. Humeau, A. Buque, L. Zitvogel, G. Kroemer, *Nat. Rev. Clin. Oncol.* **2020**, *17*, 725; c) F. Martins, L. Sofiya, G. P. Sykiotis, F. Lamine, M. Maillard, M. Fraga, K. Shabafrouz, C. Ribi, A. Cairoli, Y. Guex-Crosier, T. Kuntzer, O. Michielin, S. Peters, G. Coukos, F. Spertini, J. A. Thompson, M. Obeid, *Nat. Rev. Clin. Oncol.* **2019**, *16*, 563.

[4] a) J. Nam, S. Son, K. S. Park, W. Zou, L. D. Shea, J. J. Moon, *Nat. Rev. Mater.* **2019**, *4*, 398; b) J. D. Martin, H. Cabral, T. Stylianopoulos, R. K. Jain, *Nat. Rev. Clin. Oncol.* **2020**, *17*, 251; c) M. S. Goldberg, *Nat. Rev. Cancer* **2019**, *19*, 587; d) T. Ci, W. Zhang, Y. Qiao, H. Li, J. Zang, H. Li, N. Feng, Z. Gu, *Chem. Soc. Rev.* **2022**, *51*, 2121; e) Y. Zhai, J. Wang, T. Lang, Y. Kong, R. Rong, Y. Cai, W. Ran, F. Xiong, C. Zheng, Y. Wang, Y. Yu, H. H. Zhu, P. Zhang, Y. Li, *Nat. Nanotechnol.* **2021**, *16*, 1271.

[5] a) C. Zhang, K. Pu, *Chem. Soc. Rev.* **2020**, *49*, 4234; b) Z. Zeng, C. Zhang, J. Li, D. Cui, Y. Jiang, K. Pu, *Adv. Mater.* **2021**, *33*, e2007247.

[6] a) C. Zhang, J. Huang, Z. Zeng, S. He, P. Cheng, J. Li, K. Pu, *Nat. Commun.* **2022**, *13*, 3468; b) C. Zhang, F. Gao, W. Wu, W. X. Qiu, L. Zhang, R. Li, Z. N. Zhuang, W. Yu, H. Cheng, X. Z. Zhang, *ACS Nano* **2019**, *13*, 11249; c) C. He, X. Duan, N. Guo, C. Chan, C. Poon, R. R. Weichselbaum, W. Lin, *Nat. Commun.* **2016**, *7*, 12499; d) W. Sang, Z. Zhang, Y. Dai, X. Chen, *Chem. Soc. Rev.* **2019**, *48*, 3771; e) N. Gong, Y. Zhang, X. Teng, Y. Wang, S. Huo, G. Qing, Q. Ni, X. Li, J. Wang, X. Ye, T. Zhang, S. Chen, Y. Wang, J. Yu, P. C. Wang, Y. Gan, J. Zhang, M. J. Mitchell, J. Li, X. J. Liang, *Nat. Nanotechnol.* **2020**, *15*, 1053; f) Z. Xiao, Z. Su, S. Han, J. Huang, L. Lin, X. Shuai, *Sci. Adv.* **2020**, *6*, eaay7785; g) X. Lai, X. L. Liu, H. Pan, M. H. Zhu, M. Long, Y. Yuan, Z. Zhang, X. Dong, Q. Lu, P. Sun, J. F. Lovell, H. Z. Chen, C. Fang, *Adv. Mater.* **2022**, *34*, e2106682.

[7] W. Yue, L. Chen, L. Yu, B. Zhou, H. Yin, W. Ren, C. Liu, L. Guo, Y. Zhang, L. Sun, K. Zhang, H. Xu, Y. Chen, *Nat. Commun.* **2019**, *10*, 2025.

[8] Z. Li, Y. Wang, Y. Shen, C. Qian, D. Oupicky, M. Sun, *Sci. Adv.* **2020**, *6*, eaaz9240.

[9] a) B. Dale, M. Cheng, K. S. Park, H. U. Kaniskan, Y. Xiong, J. Jin, *Nat. Rev. Cancer* **2021**, *21*, 638; b) M. Bekes, D. R. Langley, C. M. Crews, *Nat. Rev. Drug Discov.* **2022**, *21*, 181.

[10] a) T. Ravid, M. Hochstrasser, *Nat. Rev. Mol. Cell Biol.* **2008**, *9*, 679; b) J. R. Skaar, J. K. Pagan, M. Pagano, *Nat. Rev. Drug Discov.* **2014**, *13*, 889.

[11] a) A. C. Lai, C. M. Crews, *Nat. Rev. Drug Discov.* **2017**, *16*, 101; b) C. Zhang, Z. Zeng, D. Cui, S. He, Y. Jiang, J. Li, J. Huang, K. Pu, *Nat. Commun.* **2021**, *12*, 2934.

[12] a) K. Li, C. M. Crews, *Chem. Soc. Rev.* **2022**, *51*, 5214; b) R. A. Ward, S. Fawell, N. Floc'h, V. Flemington, D. McKerrecher, P. D. Smith, *Chem. Rev.* **2021**, *121*, 3297; c) C. Wang, Y. Zhang, D. Xing, R. Zhang, *Bioorg. Chem.* **2021**, *114*, 105109.

[13] a) J. Xu, J. P. Brosseau, H. Shi, *Oncogene* **2020**, *39*, 7106; b) G. Ahn, S. M. Banik, C. R. Bertozzi, *Cell Chem. Biol.* **2021**, *28*, 1072.

[14] W. Song, J. Kuang, C. X. Li, M. Zhang, D. Zheng, X. Zeng, C. Liu, X. Z. Zhang, *ACS Nano* **2018**, *12*, 1978.

[15] a) Y. Lee, J. Heo, H. Jeong, K. T. Hong, D. H. Kwon, M. H. Shin, M. Oh, G. A. Sable, G. O. Ahn, J. S. Lee, H. K. Song, H. S. Lim, *Angew. Chem. Int. Ed.* **2020**, *59*, 17548; b) A. Ryan, J. Liu, A. Deiters, *J. Am. Chem. Soc.* **2021**, *143*, 9222.

[16] a) R. D. Case, E. Piccione, G. Wolf, A. M. Benett, R. J. Lechleider, B. G. Neel, S. E. Shoelson, *J. Biol. Chem.* **1994**, *269*, 10467; b) M. Anselmi, J. S. Hub, *Sci. Rep.* **2020**, *10*, 18530.

[17] a) Q. Liu, J. Qu, M. Zhao, Q. Xu, Y. Sun, *Pharmacol. Res.* **2020**, *152*, 104595; b) X. He, C. Xu, *Cell Res.* **2020**, *30*, 660; c) E. Quintana, C. J. Schulze, D. R. Myers, T. J. Choy, K. Mordec, D. Wildes, N. T. Shifrin, A. Belwafa, E. S. Koltun, A. L. Gill, M. Singh, S. Kelsey, M. A. Goldsmith, R. Nichols, J. A. M. Smith, *Cancer Res.* **2020**, *80*, 2889.

[18] a) C. Zhang, S. He, Z. Zeng, P. Cheng, K. Pu, *Angew. Chem. Int. Ed.* **2022**, *61*, e202114957; b) Y. Cheng, A. E. Clark, J. Zhou, T. He, Y. Li, R. M. Borum, M. N. Creyer, M. Xu, Z. Jin, J. Zhou, W. Yim, Z. Wu, P. Fajtova, A. J. O'Donoghue, A. F. Carlin, J. V. Jokerst, *ACS Nano* **2022**; c) Y. Cheng, R. M. Borum, A. E. Clark, Z. Jin, C. Moore, P. Fajtova, A. J. O'Donoghue, A. F. Carlin, J. V. Jokerst, *Angew. Chem. Int. Ed.* **2022**, *61*, e202113617.

[19] Z. Zeng, C. Zhang, S. He, J. Li, K. Pu, *Adv. Mater.* **2022**, *34*, e2203246.

[20] a) L. Dardaei, H. Q. Wang, M. Singh, P. Fordjour, K. X. Shaw, S. Yoda, G. Kerr, K. Yu, J. Liang, Y. Cao, Y. Chen, M. S. Lawrence, A. Langenbucher, J. F. Gainor, L. Friboulet, I. Dagogo-Jack, D. T. Myers, E. Labrot, D. Ruddy, M. Parks, D. Lee, R. H. DiCecca, S. Moody, H. Hao, M. Mohseni, M. LaMarche, J. Williams, K. Hoffmaster, G. Caponigro, A. T. Shaw, A. N. Hata, C. H. Benes, F. Li, J. A. Engelman, *Nat. Med.* **2018**, *24*, 512; b) Y. N. Chen, M. J. LaMarche, H. M. Chan, P. Fekkes, J. Garcia-Fortanet, M. G. Acker, B. Antonakos, C. H. Chen, Z. Chen, V. G. Cooke, J. R. Dobson, Z. Deng, F. Fei, B. Firestone, M. Fodor, C. Fridrich, H. Gao, D. Grunenfelder, H. X. Hao, J. Jacob, S. Ho, K. Hsiao, Z. B. Kang, R. Karki, M. Kato, J. Larrow, L. R. La Bonte, F. Lenoir, G. Liu, S. Liu, D. Majumdar, M. J. Meyer, M. Palermo, L. Perez, M. Pu, E. Price, C. Quinn, S. Shakya, M. D. Shultz, J. Slisz, K. Venkatesan, P. Wang, M. Warmuth, S. Williams, G. Yang, J. Yuan, J. H. Zhang, P. Zhu, T. Ramsey, N. J. Keen, W. R. Sellers, T. Stams, P. D. Fortin, *Nature* **2016**, *535*, 148.

[21] S. He, J. Liu, C. Zhang, J. Wang, K. Pu, *Angew. Chem. Int. Ed.* **2022**, *61*, e202116669.

[22] a) A. Ramesh, S. Kumar, D. Nandi, A. Kulkarni, *Adv. Mater.* **2019**, *31*, e1904364; b) V. Malik, A. Ramesh, A. A. Kulkarni, *Adv. Ther.* **2021**, *4*, 2100086.

The checkpoint nano-proteolysis targeting chimeras (nano-PROTACs, NPRO) with phototherapeutic tumor regression and immunosuppressive protein degradation are developed for activatable cancer photo-immunotherapy. NPRO-mediated therapy can not only improve tumor immunogenicity but also degrade SHP2 to block the immunosuppressive checkpoint signaling pathways (CD47/SIRPα and PD-1/PD-L1), resulting in the activation of a synergistic antitumor immune response.

Chi Zhang, Mengke Xu, Shasha He, Jingsheng Huang, Cheng Xu, and Kanyi Pu*

**Checkpoint Nano-PROTACs for Activatable Cancer Photo-immunotherapy**

TOC figure